Fluid–Structure Interaction 13

13.1 Introduction

Fluid-structure interaction is an interdisciplinary subject of interest to many research-ers in the field of fluid dynamics. The finite element method has been at the forefront of research in this important area. Fluid-structure interaction exists in its various forms in both natural systems and man-made objects. The interaction between a tree and wind and groundwater interaction with the soil are typical examples of fluid-structure interaction in nature. Fluid-structure interaction for engineered systems occurs in modeling behavior of offshore platforms with the ocean, flight characteristics of aircraft, and dams with reservoirs. Although the nature and the interaction between the solid and fluid in these problems are different, all these problems come under the category of fluid-structure interaction. It is also important to note that the degree of severity in interaction between the solid and fluid varies between different problems. While many problems involve solid deformation as an integral part, there are many man-made problems in which the solid may be considered to move as a rigid body. It is also possible to have one-directional coupling between the fluid and solid in certain problems. For the sake of completeness and clarity, we classify the subject below.

The subject may be divided into two categories based on the flow physics as (a) gas and (b) liquid interaction with solids. While incompressible flow assumption is always made for liquid-solid interaction, both compressible and incompressible flow assump-tions are made when a gas interacts with a solid. When the Mach number of flow is under 0.3, an incompressible flow assumption is justified for gas-solid interaction. The main application of air-solid interaction is in the determination of aerodynamic forces on structures such as aircraft wings. Such study is often referred to as aeroelas-ticity. Static aeroelasticity involves the study of the interaction between aerodynamic and elastic forces, while dynamic aeroelasticity is the topic that normally investigates the interaction between aerodynamic, elastic, and inertial forces. Aerodynamic flutter is one of the severe consequences of dynamic aerodynamic forces and responsible for destructive effects in aircrafts and other structures. The infamous example of the Tacoma bridge collapse is historical evidence for the destructive nature of flutter and a constant reminder of the importance of fluid-structure interaction.

The subject may also be classified based on the nature of the structure interacting with a fluid as (a) rigid body and (b) deforming body interaction with the fluid. Examples where rigid body interaction may often be used include internal combustion engines, gas and water turbines, ships, and offshore platforms. Although the rigid body–fluid interaction problem is simpler to some extent, the dynamics of rigid body motion requires a solution that reflects the fluid forces. Examples of deforming body–fluid interaction include aeroelasticity, a majority of biomedical applications, and poroelasticity. Both the rigid body and deforming body interaction with a fluid is often strongly coupled, influencing both fluid and solid forces. Within the deformable body–fluid interaction, the nature of the deforming body may vary from very simple linear elastic models in small strain to highly complex nonlinear deformations of inelastic materials. The material may also be compressible or nearly incompressible in nature.

In addition to the classification based on the physical nature of the problems, the fluid–structure interaction may also be classified based on the solution procedure employed. These classifications include (a) a monolithic approach in which both fluid and solid are treated as one unified system and (b) a partitioned approach in which the fluid and solid are treated as two different systems coupled through the interface. A partitioned approach is often preferred in practical engineering applications as this method allows the use of independently developed and tested solvers for fluids and solids. Within the partitioned approach the coupling between the fluid and solid may be carried out using a strongly or weakly coupled approach. Although the weakly coupled approach is used in aerodynamic applications, it is seldom used in other areas due to instability issues. Thus, a strongly coupled approach is the one that is preferred by most researchers. This obviously leads to various issues of coupling procedures at the interface between the fluid and solid.

Due to the emergence of immersed boundary methods in the last two decades, a further classification based on immersed boundary methods or nonconforming mesh methods may also be used. In an immersed boundary method the structure is assumed to be immersed into the fluid and the forces are transferred between fluid and solid boundaries. Since only interface forces require transferring, the need for conforming meshes is eliminated in such methods. These methods are useful in complex problems of fluid–structure interaction in which complex mesh regeneration may be difficult to carry out.

13.2 One-dimensional fluid–structure interaction

13.2.1 Equations

Fluid–structure interaction in its simplest form occurs in flexible pipes or pipe networks. In addition to normal engineering applications, a network of flexible pipes can be used to approximate blood circulation within an arterial vessel system. Since the one-dimensional fluid–structure interaction is simple to understand and implement, this is studied here first before investigating multidimensional fluid–structure
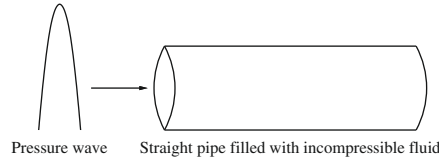
FIGURE 13.1

Flow through a flexible pipe.

interaction problems. To introduce the formulation, consider a simple problem of a flexible straight pipe as shown in Fig. 13.1. With a pressure wave passing through the flexible pipe, the surface is expected to stretch radially. By assuming only one-dimensional incompressible fluid flow and radial stretch of the flexible wall, the equations governing the cross-sectional area and velocity may be derived by reducing the continuity and momentum equations to

$$\frac{\partial A}{\partial t} + \frac{\partial (Au)}{\partial x} = 0 \tag{13.1}$$

and

$$\frac{\partial u}{\partial t} + u\frac{\partial u}{\partial x} + \frac{1}{\rho}\frac{\partial p}{\partial x} - \frac{1}{\rho}\frac{\partial \tau}{\partial r} = 0 \tag{13.2}$$

where A is cross-sectional area, t is time, u is velocity, x is axis direction, ρ is density of the fluid, p is pressure, τ is shear stress, and r is radial direction. Shear stress for a fully developed flow may be given as $\tau = \mu(\frac{\partial u}{\partial r})|_R$. Using Poiseuille flow assumptions, the shear stress may be expressed as

$$\frac{d\tau}{dr} = -\frac{8\pi \mu u}{A} \tag{13.3}$$

This is a reasonable approximation for laminar and Newtonian flows. Substituting the approximation for the shear stress, Eq. (13.2) may now be written as

$$\frac{\partial u}{\partial t} + u\frac{\partial u}{\partial x} + \frac{1}{\rho}\frac{\partial p}{\partial x} + \frac{8\pi \mu u}{\rho A} = 0 \tag{13.4}$$

The system of conservation of mass and momentum equations may now be written as

$$\frac{\partial \mathbf{\Phi}}{\partial t} + \frac{\partial \mathbf{F}}{\partial x} + \mathbf{Q} = \mathbf{0} \tag{13.5}$$

where $\mathbf{\Phi} = \begin{Bmatrix} A \\ u \end{Bmatrix}$, $\mathbf{F} = \begin{Bmatrix} uA \\ \frac{u^2}{2} + \frac{p}{\rho} \end{Bmatrix}$, and $\mathbf{Q} = \begin{Bmatrix} 0 \\ \frac{8\pi \mu}{\rho}\frac{u}{A} \end{Bmatrix}$.

Since there are three variables (A, u, and p), a third equation is required to close the system. This may be achieved through a constitutive equation that describes how pipe (or vessel) area varies with pressure and thus deals with the fluid–structure interaction

of the problem. In arterial vessel systems many different relationships are available and may be categorized as linear elastic models [1,2], where pressure is linearly related to area; nonlinear elastic models [3–17] where this relation is nonlinear; collapsible tube models [18–20], where special effort is made to accommodate tubes that can collapse as well as distend; and viscoelastic models [5,21,22], which account for the viscoelasticity of the vessel wall. While the viscoelastic models are the most complete, they are also the most complicated. Since the effects of wall viscosity are generally small, a nonlinear elastic relation is often sufficient.

The most common elastic relation used in studies of this type is that used by Formaggia et al. [23], Olufsen [12], and others and is written here (following [8,23]) as

$$p = p_{ext} + \beta \left(\sqrt{A} - \sqrt{A_0} \right) \tag{13.6}$$

where p_{ext} is external pressure, A_0 is area at zero transmural pressure (i.e., $p = p_{ext}$ or $A = A_0$), and β accounts for material properties of the elastic vessel:

$$\beta = \frac{\sqrt{\pi} h E}{A_0 (1 - \sigma^2)} \tag{13.7}$$

where h is vessel wall thickness, E is Young's modulus of the material, and σ is Poisson's ratio. All of these parameters are assumed to be independent of transmural pressure. Note that Eq. (13.6) may be rewritten in terms of wave speed as follows:

$$p = p_{ext} + 2\rho c^2 \left(1 - \sqrt{\frac{A_0}{A}} \right) \tag{13.8}$$

The intrinsic wave speed of the pipe is related to β via

$$c_0 = \sqrt{\frac{\beta \sqrt{A_0}}{2\rho}} = \sqrt{\frac{h E}{2\rho R_0 \left(1 - \sigma^2 \right)}} \tag{13.9}$$

where the second expression is called the Moens-Korteweg equation (with $A_0 = \pi R_0^2$ where R_0 is the vessel radius) and relates the material properties of the vessel to its intrinsic longitudinal wave speed, that is, the speed at which an infinitesimally small pulse would propagate in an *initially unstressed* (i.e., $A(x, 0) = A_0$) pipe. Infinitesimally small pulses in *initially stressed* (i.e., $A(x, 0) = A$) pipes propagate at a slightly different speed,

$$c = \sqrt{\frac{\beta \sqrt{A}}{2\rho}} \tag{13.10}$$

Note that finite amplitude pulses do not propagate at a speed c, but at $|u + c|$, as will be discussed in Section 13.2.2. As a consequence, the peak of a pressure wave propagates faster than its foot which would inevitably lead to shock formation in a long enough tube.

13.2.2 Characteristic analysis

The system of Eq. (13.5) is nonlinear and highly coupled, making direct analytical solutions difficult. Thus, a numerical solution is required. However when implementing a numerical solution procedure, it is useful to have a linearized decoupled form of the equations which can be used when applying boundary conditions. Following the work of Formaggia et al. [4] and Sherwin et al. [8], the system is first written in quasi-linear form, which is then used to derive the characteristic system. By taking the spatial derivative of Eq. (13.8),

$$\frac{\partial p}{\partial x} = \frac{\partial p_{ext}}{\partial x} + \frac{\beta}{2\sqrt{A}}\frac{\partial A}{\partial x} - \frac{\beta}{2\sqrt{A_0}}\frac{\partial A_0}{\partial x} + \left(\sqrt{A} - \sqrt{A_0}\right)\frac{\partial \beta}{\partial x} \tag{13.11}$$

the number of independent variables in the momentum equation can be reduced by replacing $\frac{\partial p}{\partial x}$ with Eq. (13.11). Substituting into Eq. (13.5) and rearranging, the quasi-linear form becomes

$$\frac{\partial \boldsymbol{\Phi}}{\partial t} + \mathbf{A}\frac{\partial \boldsymbol{\Phi}}{\partial x} = \mathbf{S} \tag{13.12}$$

where

$$\boldsymbol{\Phi} = \begin{bmatrix} A \\ u \end{bmatrix}, \quad \mathbf{A} = \begin{bmatrix} u & A \\ \frac{\beta}{2\rho\sqrt{A}} & u \end{bmatrix}$$

$$\mathbf{S} = -\frac{1}{\rho}\begin{bmatrix} 0 \\ 8\pi\mu\frac{u}{A} + \frac{\partial p_{ext}}{\partial x} - \frac{\beta}{2\sqrt{A_0}}\frac{\partial A_0}{\partial x} + \left(\sqrt{A} - \sqrt{A_0}\right)\frac{\partial \beta}{\partial x} \end{bmatrix}$$

The eigenvalues ($\boldsymbol{\Lambda}$) of Eq. (13.12) are given by $|\boldsymbol{\Lambda}I - \mathbf{A}| = 0$ [24]. For incompressible flows, $u < c$, so there are two real eigenvalues and the system is hyperbolic [8,25]:

$$\boldsymbol{\Lambda} = \begin{bmatrix} \lambda_f \\ \lambda_b \end{bmatrix} = u \pm \sqrt{\frac{\beta\sqrt{A}}{2\rho}} = \begin{bmatrix} u + c \\ u - c \end{bmatrix} \tag{13.13}$$

where c is the wave speed given in Eq. (13.10) and subscripts f and b represent respectively the forward and backward pointing characteristics.

Example 13.1. Derivation of characteristic variables

The characteristic speeds given in Eq. (13.13) may now be used to derive the characteristic variables. The characteristic variables and the primitive variables u and A are related via the eigenmatrix, i.e.,

$$\frac{\partial \mathbf{W}}{\partial \boldsymbol{\Phi}} = \mathbf{L} \quad \text{with} \quad \mathbf{W} = \begin{bmatrix} w_f \\ w_b \end{bmatrix} \tag{13.14}$$

where subscripts f and b, respectively, indicate the forward- and backward-moving characteristic variables. Equation (13.12) may now be transformed by multiplying Eq. (13.14) as

$$\mathbf{L}\frac{\partial \boldsymbol{\Phi}}{\partial t} + \mathbf{LA}\frac{\partial \boldsymbol{\Phi}}{\partial x} = \mathbf{LS} \tag{13.15}$$

or

$$\frac{\partial \mathbf{W}}{\partial t} + \mathbf{LAL}^{-1} \frac{\partial \mathbf{W}}{\partial x} = \mathbf{LS} \tag{13.16}$$

Since characteristic variables travel along the characteristic lines λ_1 and λ_2 of the system, the eigenvalues of Eq. (13.13) may also be expressed as $\mathbf{LAL}^{-1} = \Lambda$. From this relationship, a set of left eigenvectors may be derived using $\mathbf{l}_i \mathbf{A} = \lambda_i \mathbf{l}_i$, which leads to the left eigenmatrix. Substituting the first eigenvalue into this relationship gives

$$\begin{bmatrix} l_1 & l_2 \end{bmatrix} \begin{bmatrix} u & A \\ \frac{c^2}{A} & u \end{bmatrix} = \begin{bmatrix} l_1 & l_2 \end{bmatrix} (u + c) \tag{13.17}$$

From the above system we can write $l_1 = (c/A)l_2$. Using $l_2 = 1$ and $l_1 = (c/A)$ satisfies both equations of the system. Similarly, the left eigenvector for the second characteristic variable $(u - c)$ may be calculated as $l_1 = -(c/A)$ and $l_2 = 1$. The eigenmatrix $\mathbf{L}$ may thus be written as

$$\mathbf{L} = \begin{bmatrix} \mathbf{l}_1^T \\ \mathbf{l}_2^T \end{bmatrix} = \begin{bmatrix} \frac{c}{A} & 1 \\ -\frac{c}{A} & 1 \end{bmatrix} \tag{13.18}$$

Using Eq. (13.14), we have

$$d\mathbf{W} = \mathbf{L} \, d\mathbf{\Phi} \tag{13.19}$$

or

$$d \begin{Bmatrix} w_f \\ w_b \end{Bmatrix} = \begin{bmatrix} \frac{c}{A} & 1 \\ -\frac{c}{A} & 1 \end{bmatrix} d \begin{Bmatrix} A \\ u \end{Bmatrix} \tag{13.20}$$

Substituting Eq. (13.10) and integrating between initial (subscript 0) and instantaneous values gives

$$\begin{Bmatrix} w_f \\ w_b \end{Bmatrix} = \begin{Bmatrix} u - u_o + 4(c - c_0) \\ u - u_o - 4(c - c_0) \end{Bmatrix} = \begin{Bmatrix} w_f^* - w_f^0 \\ w_b^* - w_b^0 \end{Bmatrix} \tag{13.21}$$

where $w_{f,b}^* = u \pm 4c$ and $w_{f,b}^0 = u_o \pm 4c_0$. Since $\mathbf{S}$ in Eq. (13.16) is approximately equal to zero near the boundaries, the characteristic variables of Eq. (13.21) satisfy

$$\frac{\partial w_{f,b}}{\partial t} + \lambda_{f,b} \frac{\partial w_{f,b}}{\partial x} = 0 \tag{13.22}$$

The primitive variables can be calculated from the characteristic variables by adding or subtracting the two equations in Eq. (13.21), giving

$$A = \left[\frac{(w_f - w_b)}{8} + c_0 \right]^4 \left(\frac{2\rho}{\beta} \right)^2 \tag{13.23}$$

$$u = u_0 + \tfrac{1}{2} \left(w_f + w_b \right) \tag{13.24}$$

Figure 13.2 schematically represents the forward- and backward-running characteristic variables. The figure also shows the direction of incoming wavefronts using dashed arrows and outgoing wavefronts using solid arrows.
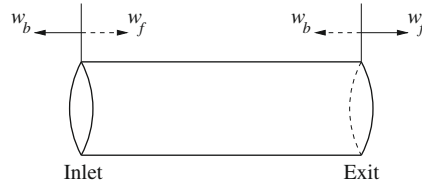
FIGURE 13.2

Nonreflecting boundary conditions in a one–dimensional domain. Solid arrow lines represent the outgoing characteristic and dashed arrow lines represent the incoming characteristic.

13.2.3 Boundary conditions

From the characteristic system discussed previously, it is obvious that the pressure and velocity *wavefronts* propagate forwards at a speed of $u + c$ [see Eq. (13.13)] and backwards at $u - c$. A "wavefront" strictly refers to an infinitesimal change in one of the characteristic variables, w_f or w_b (see Fig. 13.2). Forward-running wavefronts are initially generated by a disturbance at the inlet. These wavefronts, which compose the forward-running pressure wave, then propagate throughout the domain. To obtain a nonreflective condition at the boundaries, Eqs. (13.23) and (13.24) should be satisfied. Thus, both the forward- and backward-running wavefronts (w_f and w_b) should be computed at every time step using any prescribed condition.

Since $u < c$, $\lambda_f > 0$ and $\lambda_b < 0$ (i.e., the system is subsonic), and so one boundary condition must be specified at both the inlet and outlet. In both cases, the outgoing characteristic may be calculated via linear extrapolation in the *x-t* plane, where for the next time step $n + 1$,

$$w_b^{n+1}\Big|_{x=x_0} = w_b^n\Big|_{x=x_0-\lambda_b^n \Delta t} \tag{13.25}$$

and

$$w_f^{n+1}\Big|_{x=x_L} = w_f^n\Big|_{x=x_L-\lambda_f^n \Delta t} \tag{13.26}$$

at the inlet and outlet, respectively, where x_0 and x_L are the coordinates of the inlet and outlet. Since the governing equations (13.12) are written only in terms of cross-sectional area and velocity, one of these values or pressures should be prescribed at a boundary. All the remaining unknowns at the boundary should be computed using the wavefronts and Eqs. (13.23) and (13.24).

13.2.3.1 *Prescribed forward area, pressure, and velocity*

Prescribing the *forward* component of a variable can be achieved by prescribing the incoming characteristic (w_1) [4]. The actual values assigned to both A_{in} and u_{in} are determined at runtime based on the prescribed incoming characteristic and the current value of the outgoing characteristic [from Eq. (13.25)] which is not known *a priori*. Thus, the outgoing characteristic variable is often retained at the initial value when

applying boundary conditions. To prescribe the forward area, rearrange (13.23) to give at the inlet

$$w_f^{*n+1} = w_b^{*0} + 8 \left(\bar{A}^{n+1} \right)^{1/4} \sqrt{\frac{\beta}{2\rho}} \tag{13.27}$$

Note that $w_{f,b}^*$ are defined in Eq. (13.21). Similarly, to prescribe the forward pressure, substitute (13.6) into (13.27):

$$w_f^{*n+1} = w_b^{*0} + 4 \sqrt{\frac{2}{\rho}} \sqrt{\left(\bar{p}^{n+1} - p_{ext} \right) + \beta \sqrt{A_0}} \tag{13.28}$$

Finally, the forward velocity may be prescribed by rearranging (13.24):

$$w_f^{*n+1} = 2\bar{u}^{n+1} - w_b^{*0} \tag{13.29}$$

In these equations, w_b^{*0} is the initial value of w_b^* and is also equal to the value of w_b^* at any time if no backward-running waves reach the inlet. If not given, the values of A_{in}^{n+1} and u_{in}^{n+1} may be calculated from Eqs. (13.25), (13.26), (13.23), and (13.24). Since prescribing the forward component of a variable using a forward-moving characteristic variable is more physically intuitive, this approach will be adopted in this section unless otherwise stated. Prescribing *backward* components of the variables at the outlet could also be achieved in a similar manner.

13.2.4 Solution method: Taylor-Galerkin method

Standard Galerkin discretization of Eq. (13.5) leads to spatial instability in the presence of the dominant convective term. One possible way of achieving better spatial stability is by including the Taylor-Galerkin stabilization. In this method, Eq. (13.5) is used to obtain a semi-discrete form using the Taylor expansion. We rewrite the governing equation as

$$\frac{\partial \mathbf{\Phi}}{\partial t} = -\mathbf{Q} - \frac{\partial \mathbf{F}}{\partial x} \tag{13.30}$$

where $\mathbf{\Phi}$, $\mathbf{F}$, and $\mathbf{Q}$ are vectors of primitive variables, fluxes, and source terms, respectively. Differentiating Eq. (13.30) with respect to time and applying the chain rule,

$$\frac{\partial^2 \mathbf{\Phi}}{\partial t^2} = -\mathbf{S} \frac{\partial \mathbf{\Phi}}{\partial t} - \frac{\partial}{\partial x} \left(\mathbf{A} \frac{\partial \mathbf{\Phi}}{\partial t} \right) \tag{13.31}$$

where $\mathbf{A} = \dfrac{\partial \mathbf{F}}{\partial \mathbf{\Phi}}$ and $\mathbf{S} = \dfrac{\partial \mathbf{Q}}{\partial \mathbf{\Phi}}$. Substituting Eq. (13.30) into Eq. (13.31) removes the time derivatives from the right-hand side, i.e.,

$$\frac{\partial^2 \mathbf{\Phi}}{\partial t^2} = \mathbf{S} \left(\mathbf{Q} + \frac{\partial \mathbf{F}}{\partial x} \right) + \frac{\partial (\mathbf{AQ})}{\partial x} + \frac{\partial}{\partial x} \left(\mathbf{A} \frac{\partial \mathbf{F}}{\partial x} \right) \tag{13.32}$$

The Taylor series expansion of Φ^{n+1} in time is

$$\Phi^{n+1} = \Phi^n + \Delta t \frac{\partial \Phi^n}{\partial t} + \frac{1}{2}\Delta t^2 \frac{\partial^2 \Phi^n}{\partial t^2} + O\left(\Delta t^3\right) \qquad (13.33)$$

where Δt is the time step and n refers to the current time step. Ignoring third- and higher-order terms, and substituting Eqs. (13.30) and (13.31) into Eq. (13.33) yields the final explicit semi-discrete form as

$$\frac{\Phi^{n+1} - \Phi^n}{\Delta t} = -\mathbf{Q}^n - \frac{\partial \mathbf{F}^n}{\partial x} + \frac{1}{2}\Delta t \left[\frac{\partial}{\partial x}\left(\mathbf{A}^n\mathbf{Q}^n + \mathbf{A}^n\frac{\partial \mathbf{F}^n}{\partial x}\right) + \mathbf{S}^n\frac{\partial \mathbf{F}^n}{\partial x} + \mathbf{S}^n\mathbf{Q}^n \right] \qquad (13.34)$$

Note that the second bracketed term is the Taylor-Galerkin stabilization term. Now, application of standard Galerkin weighting along with the application of conditional stability on the time step provides a stable solution.

The standard spatial discretization for the finite element method is performed over the global domain Ω which has boundaries denoted by Γ. The Galerkin weighting $\mathbf{N}^T$ along with a linear spatial discretization provides a residual equation which converges to the exact solution when the element size approaches zero, that is,

$$\int_\Omega \left(\mathbf{N}^T \frac{\Delta \hat{\Phi}^n}{\Delta t} - \mathbf{N}^T \hat{\mathbf{R}}^n\right) d\Omega = 0 \qquad (13.35)$$

where $\hat{\mathbf{R}}$ is the right-hand side of Eq. (13.34). The hat signifies that these variables are approximated by the finite element method, where for any variable Φ, for example, $\hat{\Phi} = N_a\tilde{\Phi}_a + N_b\tilde{\Phi}_b = \mathbf{N}\tilde{\Phi}$ means that the value of $\hat{\Phi}$ anywhere in a given one-dimensional element is interpolated between two discrete nodes (a, b) with nodal values $\tilde{\Phi}_a$ and $\tilde{\Phi}_b$ using the linear interpolation functions $N_a = (x_b - x)/(x_b - x_a)$ and $N_b = (x - x_a)/(x_b - x_a)$. Evaluation of Eq. (13.35) results in the following equation in compact matrix form:

$$\mathbf{M}\Delta\Phi = \Delta t \left(\mathbf{K}\mathbf{F}^n - \mathbf{L}\mathbf{Q}^n + \mathbf{f}^n\right) \qquad (13.36)$$

where $\mathbf{M}$ is called the mass matrix and $\mathbf{K}$ and $\mathbf{L}$ are coefficient matrices for convection, Taylor-Galerkin, and source terms; each of these are $N_{nodes} \times N_{nodes}$ matrices, where N_{nodes} is the number of nodes in Ω. Also, $\Delta\Phi = \Phi^{n+1} - \Phi^n$ and $\mathbf{f}$ contains boundary fluxes and boundary conditions. The element matrices for a linear element inside the domain are given below.

The element mass matrix is

$$\mathbf{M}_e = \frac{l_e}{6}\begin{bmatrix} 2 & 1 \\ 1 & 2 \end{bmatrix} \qquad (13.37)$$

where l_e is the element length. The lumped mass matrix

$$\mathbf{M}_e^L = \frac{l_e}{2}\begin{bmatrix} 1 & 0 \\ 0 & 1 \end{bmatrix} \qquad (13.38)$$

may also be used.

The convection term is integrated by parts over an element as

$$-\int_{\Omega_e} \mathbf{N}^T \frac{\partial \hat{\mathbf{F}}^n}{\partial x}\, d\Omega_e = \int_{\Omega_e} \frac{\partial \mathbf{N}^T}{\partial x} \hat{\mathbf{F}}^n\, d\Omega_e - \int_{\Gamma_e} \mathbf{N}^T \hat{\mathbf{F}}^n \mathbf{n}\, d\Gamma_e \qquad (13.39)$$

The last term in the above equation is active only for elements at the boundaries. Similarly the Taylor-Galerkin term is integrated by parts, giving

$$\int_{\Omega_e} \mathbf{N}^T \frac{\partial}{\partial x}\left(\mathbf{A}^n \frac{\partial \hat{\mathbf{F}}^n}{\partial x}\right) d\Omega_e = -\int_{\Omega_e} \frac{\partial \mathbf{N}^T}{\partial x} \mathbf{A}^n \frac{\partial \hat{\mathbf{F}}^n}{\partial x}\, d\Omega_e + \int_{\Gamma_e} \mathbf{N}^T \bar{\mathbf{A}}^n \frac{\partial \hat{\mathbf{F}}^n}{\partial x}\, d\Gamma_e$$
$$(13.40)$$

Evaluation of Eqs. (13.39) and (13.40) provides the coefficient matrix $\mathbf{K}_e$ for the inviscid case. If a source term is also included, the full matrix is found to be

$$\mathbf{K}_e = \left(\frac{1}{2} - \frac{\Delta t}{4}\breve{\mathbf{S}}^n\right)\begin{bmatrix} -1 & -1 \\ 1 & 1 \end{bmatrix} - \frac{\Delta t}{2l_e}\breve{\mathbf{A}}^n\begin{bmatrix} 1 & -1 \\ -1 & 1 \end{bmatrix} \qquad (13.41)$$

where $\breve{\mathbf{A}}$ and $\breve{\mathbf{S}}$ are the average values over the element subdomain. This is an alternative to numerical integration, which is equivalent when using linear shape functions. Similarly the coefficient matrix $\mathbf{L}_e$ is found to be

$$\mathbf{L}_e = \left(\frac{l_e}{6} - \frac{\Delta t l_e}{12}\breve{\mathbf{S}}^n\right)\begin{bmatrix} 2 & 1 \\ 1 & 2 \end{bmatrix} + \frac{\Delta t}{4}\breve{\mathbf{A}}^n\begin{bmatrix} -1 & -1 \\ 1 & 1 \end{bmatrix} \qquad (13.42)$$

For the flux term, the contributions from the Taylor-Galerkin terms are not included since these arise from the numerical technique and will be zero on the boundaries. Thus, for the elements at the boundaries (if applicable),

$$\mathbf{f}_e = \begin{Bmatrix} \tilde{\hat{\mathbf{F}}}_a^n \\ -\tilde{\hat{\mathbf{F}}}_b^n \end{Bmatrix} \qquad (13.43)$$

The system can then be implemented by assembling and substituting Eqs. (13.37) and (13.41)–(13.43) into Eq. (13.36) and adding the boundary conditions (see Section 13.2.3). Assuming that $u \ll c$, it can be shown that the stability condition for the characteristic system in Section 13.2.2 is [15,20]

$$\Delta t_{max} \approx \frac{\Delta x_{min}}{c_{max}} \qquad (13.44)$$

although for a nonzero source term ($\mathbf{Q}$) this will be slightly lower. Experience has shown that Eq. (13.44) with a small safety factor (i.e., using $\Delta t = 0.9\,\Delta t_{max}$) works well for the coupled system [Eq. (13.5)].

13.2.5 Some results

Only two simple examples are provided in this subsection. The practical application of one-dimensional fluid–structure interaction is discussed for a human arterial system in Chapter 14.

Example 13.2. Pulse propagation in a single uniform vessel

Figure 13.3 shows the propagation of a Gaussian pressure pulse in a single vessel with uniform initial area $A_0 = 1.0$ cm and $\beta = 229674$ dynes/cm^3. Note that the width of this pulse (0.03 s) is very short. In Fig. 13.3a it can be seen that for a relatively low amplitude pulse (10^3 dynes/cm^2) and inviscid conditions ($\mu = 0$), the pulse propagates with little distortion. Introducing viscous effects ($\mu = 0.035$ P) leads to the gradual decay of the pulse as energy is lost due to viscous friction. For a larger amplitude pressure pulse (10^4 dynes/cm^2), there is significant distortion
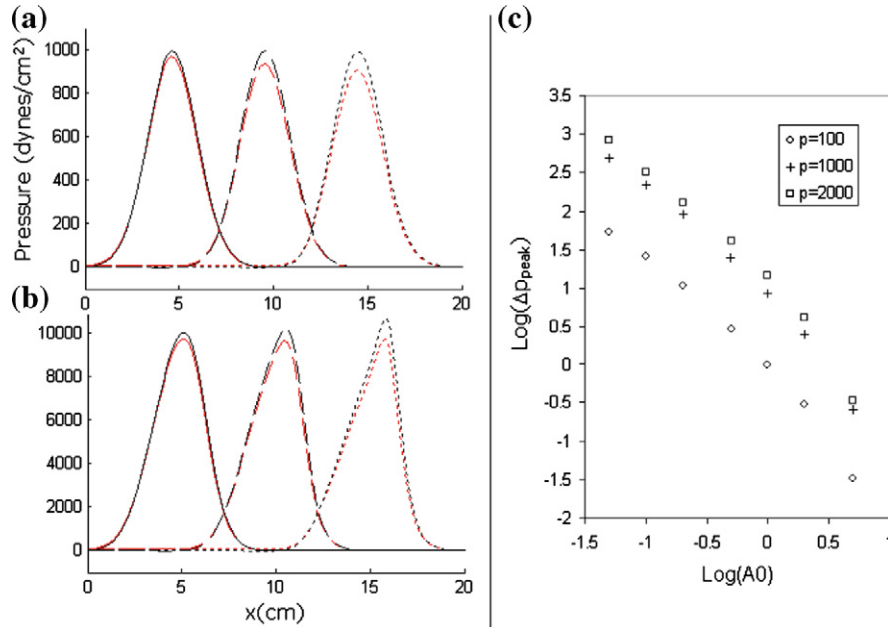

FIGURE 13.3

Propagation of a short (a) small and (b) large amplitude pressure pulse in a single vessel for inviscid (higher amplitude) and viscous flow (lower amplitude), with snapshots taken at $t = 0.03$ s (solid lines), 0.045 s (dashed lines), and 0.06 s (dotted lines). For small amplitude pulses, propagation is approximately linear and the pulse does not distort. For large amplitude pulses, nonlinear effects distort the pulse and lead to shock formation. (c) Log-log plot of pressure peak decay Δp_{peak} over 20 cm due to viscosity with different vessel cross-sectional areas (A_0) and for initial pulse amplitudes of 100, 1000, and 2000 dynes/cm^2.

(Fig. 13.3b) due to both viscous effects and nonlinear effects. As discussed in Section 13.2.1, the pressure peak propagates faster than its foot, which is predicted from Eq. (13.10). The result is that, given enough time, the high pressure peak will catch up with the low pressure foot, thus forming a shock. Since the foot propagates at c_0 and from Eq. (13.13) the peak propagates at $u_{peak} + c_{peak}$, the approximate distance at which a shock will form is 182 cm for the pulse in Fig. 13.3a and 18.4 cm for pulse in Fig. 13.3b. Fig. 13.3c shows that the attenuation of the pressure pulse due to viscosity is dependent on vessel cross-sectional area. As predicted from Eq. (13.3), the decay of the pressure peak (Δp_{peak}) is greater for small vessels or for large amplitude pulses.

Example 13.3. Discontinuities

Figure 13.4a shows the effect of a sudden decrease in A_0. Since this corresponds to an increase in characteristic impedance, there is a partial positive reflection. The linear reflection coefficient may be calculated using the characteristic impedance or admittance. Defining the characteristic impedance as

$$Z_0 = \frac{1}{Y_0} = \frac{\rho c_0}{A_0} \qquad (13.45)$$

where Y_0 is the characteristic admittance, the reflection coefficient may now be computed using

$$R = \frac{Y_{0p} - \sum_{i=1}^{n} Y_{0i}}{Y_{0p} + \sum_{i=1}^{n} Y_{0i}} \qquad (13.46)$$

where p indicates the starting vessel before the change in area, properties, or topology and n is the number of branching daughter vessels. This is only applicable when pipe or arterial networks (see Chapter 14) are considered.

The reflection coefficient calculated for the problem shown in Fig. 13.4a is $R = 0.25$, while the transmission coefficient (from transmission line theory, $T = 1 + R$) is $T = 1.25$. The amplitudes of the reflected and transmitted waves approximately
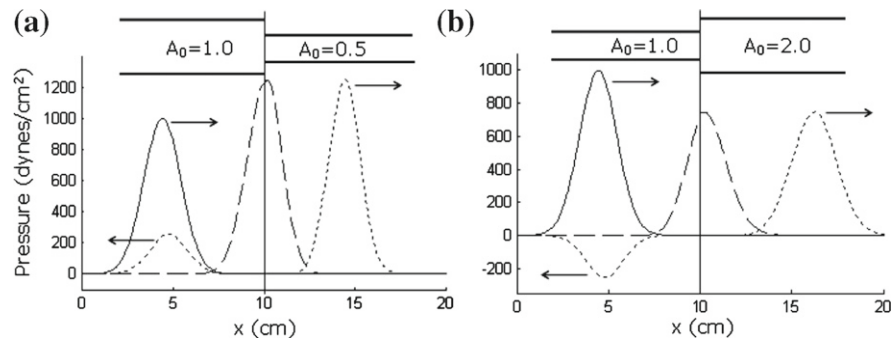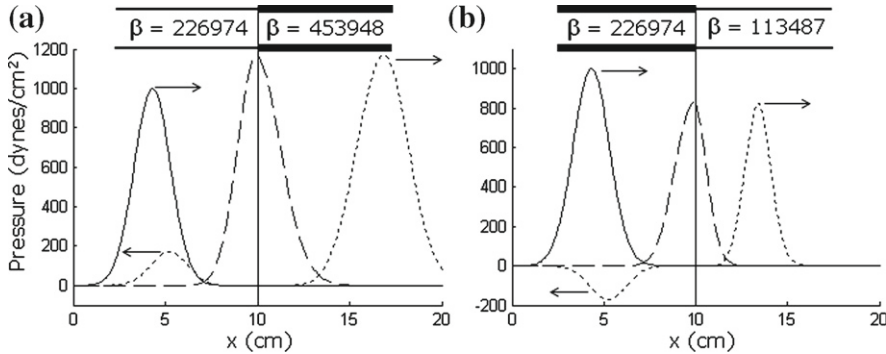

FIGURE 13.4

Reflected and transmitted waves in a single vessel due to (a) a step decrease and (b) a step increase in A_0.

FIGURE 13.5

Reflected and transmitted waves in a single vessel due to (a) a step increase and (b) a step decrease in β with constant A_0.

represent these values, and while the concept of reflection coefficient is not strictly valid for the nonlinear system, small pulses do approach the linear behavior. Conversely, Fig. 13.4b demonstrates that there is a partial negative reflection when A_0 is increased (with $R = -0.25$ and $T = 0.75$).

Another possible type of discontinuity is in β. Assuming A_0 is constant, this reflects a sudden change in material properties (Young's modulus or wall thickness) of the vessel [see Eq. (13.7)]. Figure 13.5 shows reflected and transmitted waves for a single reflection site where β doubles or halves. Note that wave speed increases or decreases along with β [Eq. (13.10)] as shown by changes in the width of the pulse.

13.3 Multidimensional problems

In the one-dimensional problem discussed in the previous section, the mesh points are fixed and the material is allowed to pass through the fixed mesh. This Eulerian approach simplified the presentation dramatically. However, in multidimensions the issue is more complicated due to an explicit interface which was absent for one-dimensional problems. Since this interface in multidimensions is not fixed, the problem for fluid dynamics becomes a moving boundary problem. In addition the interface forces should be exchanged between the two media in a sensible way to couple the two domains. In the following sections we use an incompressible fluid as a model problem to describe the fluid–structure interaction. The methods presented are equally valid for compressible flows.

13.3.1 Equations and discretization

With reference to Fig. 13.6, the incompressible flow equations governing the flow inside the fluid domain may be written in nonconservation form and in arbitrary
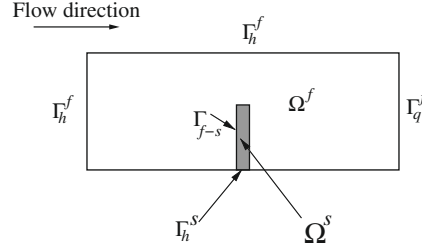
FIGURE 13.6

Schematic of a fluid–structure interaction problem. Superscripts f and s respectively indicate the fluid and solid and subscripts h, q, and $f-s$ respectively indicate a Dirichlet, Neumann, and fluid–structure interface boundary.

Lagrangian and Eulerian (ALE) frame as follows (refer to Chapter 6):

$$\rho_f \left(\frac{\partial u_i}{\partial x_i} + (u_j - u_j^g) \frac{\partial u_i}{\partial x_j} \right) = -\frac{\partial p}{\partial x_i} + \frac{\partial \tau_{ij}}{\partial x_j} \tag{13.47}$$

is the momentum equation with the deviatoric stresses τ_{ij} expressed as

$$\tau_{ij} = \mu \left(\frac{\partial u_i}{\partial x_j} + \frac{\partial u_j}{\partial x_i} \right) \tag{13.48}$$

and the conservation of mass equation in the domain is given as

$$\frac{\partial u_i}{\partial x_i} = 0 \tag{13.49}$$

The flow problem is completed using the following boundary conditions:

$$u_i = \bar{u}_i \quad \text{on} \quad \Gamma_h^f$$
$$t_i^f = \tau_{ij} n_j - p n_i = \bar{t}_i^f \quad \text{on} \quad \Gamma_q^f$$
$$u_i = \frac{\mathrm{d} d_i}{\mathrm{d} t} = \dot{d}_i \quad \text{on} \quad \Gamma_{f-s} \tag{13.50}$$

where t_i are the components of traction, quantities with the overbar are assumed to be known, and d_i are the components of displacement at the fluid–solid interface. This condition applied at the interface is referred to as the kinematic condition.

For simplicity, in the treatment of the solid body we consider only the small deformation form described in Ref. [26]. This includes all the salient features of the fluid–structure interaction problem without the need to treat the more complex finite deformation effects. Accordingly, the momentum equation for the solid may be written as

$$\rho_s \frac{\partial^2 d_i}{\partial t^2} - \frac{\partial \sigma_{ij}}{\partial x_j} = f_i \tag{13.51a}$$

in which the stress σ_{ij} for a linear isotropic elastic material is related to strains as

$$\sigma_{ij} = \lambda\delta_{ij}\frac{\partial d_k}{\partial x_k} + \mu\left(\frac{\partial d_i}{\partial x_j} + \frac{\partial d_j}{\partial x_i}\right) \tag{13.51b}$$

where λ, μ are the Lamè elastic constants, δ_{ij} is the Kronecker delta, ρ_s is the density of the solid, and f_i are the body force components. The boundary conditions for the solid domain may now be written as

$$d_i = \bar{d}_i \quad \text{on} \quad \Gamma_h^s$$
$$t_i^s = \sigma_{ij}n_j = \bar{t}_i^s \quad \text{on} \quad \Gamma_q^s$$
$$(\sigma_{ij}n_j)^s - (\tau_{ij}n_j - pn_i)^f = 0 \quad \text{or} \quad t_i^s + t_i^f = 0 \quad \text{on} \quad \Gamma_{f-s} \tag{13.52}$$

The condition imposed at the interface in Eq. (13.52) is often referred to as the dynamic condition. Equations (13.47)–(13.52) form the governing equation system for fluid–structure interaction.

13.3.1.1 *Finite element formulation of fluid equations*

The finite element algorithms and spatial discretization are extensively discussed in Chapters 2 and 3. Although any of the standard fluid dynamics algorithm can be used, we use the CBS scheme as the basis to explain the monolithic form [27–30]. In order to establish this, we use Section 3.6 of Chapter 3. Assuming that the flow is unsteady, Eq. (3.51) (Step 1 of the CBS scheme) may be written for a generic incompressible flow with implicit time discretization as

$$\frac{\Delta\tilde{\mathbf{U}}^\star}{\Delta t} = -\mathbf{M}_u^{-1}\left[(\mathbf{C}_u\tilde{\mathbf{U}} + \mathbf{K}_\tau\tilde{\mathbf{u}} - \mathbf{f}) - \Delta t(\mathbf{K}_u\tilde{\mathbf{U}} + \mathbf{f}_s)\right]^{n+1} \tag{13.53}$$

Similarly Steps 2 [Eq. (3.56)] and 3 [Eq. (3.59)] are written as (with $\theta_1 = 1$ and $\theta_2 = 1$)

$$(\Delta t\mathbf{H})\tilde{\mathbf{p}}^{n+1} = [\mathbf{G}\tilde{\mathbf{U}}^\star - \mathbf{f}_p] \tag{13.54}$$

and

$$\frac{\Delta\mathbf{U}^{\star\star}}{\Delta t} = \frac{\Delta\tilde{\mathbf{U}} - \Delta\tilde{\mathbf{U}}^\star}{\Delta t} = -\mathbf{M}_u^{-1}\left[\mathbf{G}^{\mathrm{T}}(\tilde{\mathbf{p}}^{n+1}) + \frac{\Delta t}{2}\mathbf{P}\tilde{\mathbf{p}}^{n+1}\right] \tag{13.55}$$

Although various other time integration schemes are possible, for the sake of simplicity we use $\Delta\mathbf{U}^* = \mathbf{U}^* - \mathbf{U}^n$ and $\Delta\mathbf{U} = \mathbf{U}^{n+1} - \mathbf{U}^n$. We get the following equation by substituting Eq. (13.55) into Eq. (13.53):

$$\mathbf{M}_u\tilde{\mathbf{U}}^{n+1} - \mathbf{M}_u\tilde{\mathbf{U}}^n + \left[(\mathbf{C}_u\tilde{\mathbf{U}} + \mathbf{K}_\tau\tilde{\mathbf{u}} - \mathbf{f}) - \Delta t(\mathbf{K}_u\tilde{\mathbf{U}} + \mathbf{f}_s) + \mathbf{G}^{\mathrm{T}}(\tilde{\mathbf{p}}^{n+1})\right.$$
$$\left. + \frac{\Delta t}{2}\mathbf{P}\tilde{\mathbf{p}}^{n+1}\right]^{n+1} = 0 \tag{13.56}$$

Similarly, substituting Eq. (13.55) into (13.54) gives

$$\mathbf{G}\tilde{\mathbf{U}}^{n+1} + \Delta t \mathbf{G}\mathbf{M}_u^{-1}\left[\mathbf{G}^{\mathrm{T}}(\tilde{\mathbf{p}}^{n+1}) + \frac{\Delta t}{2}\mathbf{P}\tilde{\mathbf{p}}^{n+1}\right] - \Delta t \mathbf{H}\tilde{\mathbf{p}}^{n+1} - \underset{\sim}{f}_p = \mathbf{0} \quad (13.57)$$

Equations (13.56) and (13.57) may be written in matrix form as

$$\begin{bmatrix} \mathbf{M}_u + \mathbf{K}_\tau/\rho + \mathbf{C}_u - \Delta t \mathbf{K}_u & \mathbf{G}^{\mathrm{T}} + \frac{\Delta t}{2}\mathbf{P} \\ \mathbf{G} & \Delta t[\mathbf{G}\mathbf{M}_u^{-1}\left(\mathbf{G}^{\mathrm{T}} + \frac{\Delta t}{2}\mathbf{P}\right) - \mathbf{H}] \end{bmatrix}\begin{Bmatrix} \tilde{\mathbf{U}} \\ \tilde{\mathbf{p}} \end{Bmatrix}^{n+1} = \begin{Bmatrix} \mathbf{f}_1 \\ \mathbf{f}_2 \end{Bmatrix}$$
$$(13.58)$$

Here $\mathbf{f}_1$ and $\mathbf{f}_2$ terms are the forcing terms. In the context of fluid–structure interaction, the interface dynamic condition should be included within the formulation. Thus the interface condition in Eq. (13.50) may be integrated along the interface as a Lagrange multiplier constraint and gives a functional term

$$\tilde{\boldsymbol{\lambda}}^{\mathrm{T}} \int_{\Gamma_{f-s}} \mathbf{N}_\lambda^{\mathrm{T}}(\mathbf{u} - \dot{\mathbf{d}})^{n+1}\mathrm{d}\Gamma_{f-s} = 0 \quad (13.59)$$

in which $\boldsymbol{\lambda}$ is discretized along the interface as

$$\boldsymbol{\lambda} = \mathbf{N}_\lambda \tilde{\boldsymbol{\lambda}} \quad (13.60)$$

Assuming that $\mathbf{d} = \mathbf{N}_d \tilde{\mathbf{d}}$ and with $\mathbf{u} = \mathbf{N}_u \tilde{\mathbf{u}}$, the above equation may be written for the interface nodes as

$$\tilde{\boldsymbol{\lambda}}^{\mathrm{T}}\left(\mathbf{M}_{\lambda u}^\Gamma \tilde{\mathbf{u}}^{n+1} - \mathbf{M}_{\lambda u}^\Gamma \tilde{\dot{\mathbf{d}}}^{n+1}\right) = 0 \quad (13.61)$$

where

$$\mathbf{M}_{\lambda u}^\Gamma = \int_{\Gamma_{f-s}} \mathbf{N}_\lambda^T \mathbf{N}_u \, \mathrm{d}\Gamma_{f-s}$$
$$\mathbf{M}_{\lambda d}^\Gamma = \int_{\Gamma_{f-s}} \mathbf{N}_\lambda^T \mathbf{N}_d \, \mathrm{d}\Gamma_{f-s} \quad (13.62)$$

In the case of fluid–structure interaction problems, the variation of (13.59) with respect to the fluid velocity should be added to (13.56). To put together the full system of simultaneous equations for a fluid–structure system, we need to discretize (13.51a) along with the interface condition given in (13.52).

13.3.1.2 *Finite element formulation of solid dynamics*
Following Chapter 12 of Ref. [26], we can write the semi-discrete form of the equation governing the solid dynamics as

$$\mathbf{M}_d \tilde{\ddot{\mathbf{d}}} + \mathbf{C}_d \tilde{\dot{\mathbf{d}}} + \mathbf{K}_d \tilde{\mathbf{d}} + \mathbf{f}_d = 0 \quad (13.63)$$

These may be discretized in time using several alternative methods. For one-step methods the form of (13.63) becomes

$$\left(c_3 \mathbf{M}_d + c_2 \mathbf{C}_d + c_1 \mathbf{K}_d\right)\tilde{\mathbf{d}}^{n+1} + \mathbf{f}_d^{n+1} = \mathbf{0} \quad (13.64)$$

For example in the Newmark procedure [26,31,32], the solution is advanced using

$$\tilde{\mathbf{d}}^{n+1} = \tilde{\mathbf{d}}^n + \Delta t \dot{\tilde{\mathbf{d}}}^n + \left(\tfrac{1}{2} - \beta\right) \Delta t^2 \ddot{\tilde{\mathbf{d}}}^n + \beta \Delta t^2 \ddot{\tilde{\mathbf{d}}}^{n+1}$$

$$\dot{\tilde{\mathbf{d}}}^{n+1} = \dot{\tilde{\mathbf{d}}}^n + (1 - \gamma)\Delta t \ddot{\tilde{\mathbf{d}}}^n + \gamma \Delta t \ddot{\tilde{\mathbf{d}}}^{n+1}$$

where β and γ are parameters controlling accuracy and stability and the c_i parameters are given by

$$c_1 = 1, \quad c_2 = \frac{\gamma}{\beta \Delta t} \quad \text{and} \quad c_3 = \frac{1}{\beta \Delta t^2}$$

Discretization of the dynamic boundary condition at the interface given in (13.52) may be performed similar to (13.59). However, one can show that the Lagrange multiplier in (13.59) is the fluid traction (see, for example, Chapter 3 of Ref. [26]) and, thus, may be used also on the solid interface to enforce nodally the dynamic boundary condition.

13.3.1.3 *Monolithic fluid–structure interaction formulation*

The monolithic form of a fluid–structure interaction system may now put together using Eqs. (13.58), (13.61), and (13.64) as

$$\begin{bmatrix} \mathbf{K}_{11} & \mathbf{K}_{12} & \mathbf{0} & \mathbf{K}_{14} \\ \mathbf{K}_{21} & \mathbf{K}_{22} & \mathbf{0} & \mathbf{0} \\ \mathbf{0} & \mathbf{0} & \mathbf{K}_{33} & \mathbf{K}_{34} \\ \mathbf{K}_{41} & \mathbf{0} & \mathbf{K}_{43} & \mathbf{0} \end{bmatrix} \begin{Bmatrix} \tilde{\mathbf{U}} \\ \tilde{\mathbf{p}} \\ \tilde{\mathbf{d}} \\ \tilde{\lambda} \end{Bmatrix}^{n+1} = \begin{Bmatrix} \mathbf{f}_1 \\ \mathbf{f}_2 \\ \mathbf{f}_3 \\ \mathbf{f}_4 \end{Bmatrix} \qquad (13.65)$$

where the nonzero entries of the above equation may be written as

$$\mathbf{K}_{11} = \mathbf{M}_u + \frac{1}{\rho}\mathbf{K}_\tau + \mathbf{C}_u - \Delta t \mathbf{K}_u$$

$$\mathbf{K}_{12} = \mathbf{G}^{\mathrm{T}} + \frac{\Delta t}{2}\mathbf{P}$$

$$\mathbf{K}_{21} = \mathbf{G}$$

$$\mathbf{K}_{22} = \Delta t \left[\mathbf{G}\mathbf{M}_u^{-1}\left(\mathbf{G}^{\mathrm{T}} + \frac{\Delta t}{2}\mathbf{P}\right) - \mathbf{H}\right]$$

$$\mathbf{K}_{33} = c_3\mathbf{M}_d + c_2\mathbf{C}_d + c_1\mathbf{K}_d$$

$$\mathbf{K}_{14} = \mathbf{M}_{\lambda u}^{\Gamma,T}$$

$$\mathbf{K}_{34} = \mathbf{M}_{\lambda d}^{\Gamma,T}$$

$$\mathbf{K}_{41} = \mathbf{M}_{\lambda u}^{\Gamma}$$

$$\mathbf{K}_{43} = \mathbf{K}_{\lambda d}^{\Gamma} \qquad (13.66)$$

It is important to note that various stabilization components including the pressure stabilization part $\mathbf{K}_{22}$ in the above equation may be replaced with different methods

of stabilization to obtain different stabilized formulations. The monolithic form, Eq. (13.65), may also be written in a single residual form as

$$\mathbf{R}(\mathbf{W}) = 0 \tag{13.67}$$

where $\mathbf{R}$ is the sum of all residuals of Eq. (13.65) and $\mathbf{W}$ are the unknowns of Eq. (13.65). In theory Eq. (13.67) can be solved using a Newton method to obtain a solution. The solution procedure may take the following form:

- Start with an initial guess for $\mathbf{W}$ equal to $\mathbf{W}^n$ at the nth time iteration.
- Using the initial guess calculate the residual at the nth time iteration as $\mathbf{R}(\mathbf{W}^n)$ and the Jacobian (or tangent) matrix $\mathbf{A} = \frac{\partial \mathbf{R}}{\partial \mathbf{W}}(\mathbf{W}^n)$
- Solve for the correction of $\Delta \mathbf{W}$ by solving the set of simultaneous equations $\mathbf{A}\Delta\mathbf{W} = \mathbf{R}(\mathbf{W}^n)$.
- Update the solution using $\mathbf{W}^{n+1} = \mathbf{W}^n + \gamma \Delta\mathbf{W}$, where γ is an optimal parameter that determines the step size. The process of determining this parameter is referred to as line search.

For more details on approximate Newton methods and the line search algorithm, readers are referred to Chapter 3 of Ref. [32].

13.3.2 Segregated approach

Although the monolithic approach discussed above is a natural and strongly coupled way of solving the FSI problems, it poses several difficulties in practice. In addition to convergence issues associated with the monolithic form, the implementation issues can also be cumbersome. The implementation difficulties are often posed by the fact that fluid and solid solvers in general are independently developed and tested. Thus, it is more practical to implement a segregated approach that combines the established fluid and solid algorithms. In such segregated approaches, the coupling is carried out through the dynamic and kinematic conditions at the interface. This provides us with two alternatives. The first one is the so-called loosely coupled approach in which the interface conditions may or may not be fully satisfied. Such loosely coupled approaches are sometime applied in aeroelasticity calculations. The second approach is the so-called strongly coupled approach in which the interface conditions are more accurately satisfied. The loosely coupled approach can be unstable for many applications, especially applications in which the solid and fluid density values are close [27]. The strong coupling may be achieved through different methods. Figure 13.7 shows a typical coupling routine. As seen, this provides a large number of different options to couple the fluid and structure [28–30,33–39].

When the fluid and solid solvers are separately available (see Fig. 13.7), the coupling between them may be carried out via Dirichlet-Neumann coupling. To understand such a coupling let us assume that the discrete form of fluid equation, Eq. (13.58), and fully discrete form of solid equation, Eq. (13.64), are
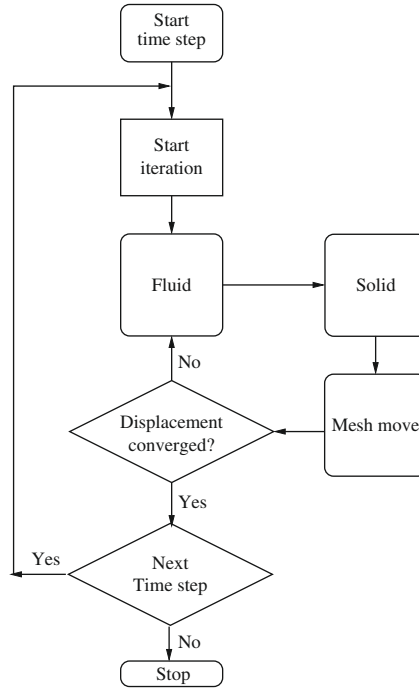
$$\mathbf{K}^f \mathbf{u}^f = \mathbf{F}^f \tag{13.68}$$

FIGURE 13.7

Strong coupling of fluid and structure solvers using a staggered approach.

and

$$\mathbf{K}^s \mathbf{d}^s = \mathbf{F}^s \tag{13.69}$$

respectively. To couple the two equations strongly, start the iteration with the initial solutions of solid and fluid variables and solve the fluid equation (13.68) to determine the new fluid variables and fluid forces at the interface. This is followed by solution to Eq. (13.69) to determine the displacements within the solid domain, calculation of fluid velocity at the interface from the interface displacements and determination of new mesh position. Now, check whether or not interface displacements converged. If not, using the interface velocity values solve the flow equation, Eq. (13.68). Continue this iteration between fluid, solid, and mesh until interface displacements are converged. The interface displacements are often converged quickly using relaxation methods.

13.3.3 Mesh moving procedures

In a majority of fluid–structure interaction problems the mesh of both solid and fluid domains is altered in one way or another. Often the solid domain is treated using a Lagrangian form of mesh movement and the fluid domain is subjected to the so-called

arbitrary Lagrangian-Eulerian (ALE) method. In an ALE formulation, the mesh is allowed to move independently of the material points. This independent motion of the mesh to maintain mesh quality in general is not necessarily always straightforward. The reason is that sophisticated methods of mesh motion are often computationally expensive. The simple methods on the other hand are not very useful for calculating large deformation of meshes. For really complex problems of practical interest, preserving the topology of the mesh and avoiding remeshing may not be possible. Thus, in addition to remeshing algorithms, a robust interpolation method to transfer variables from the original mesh to new mesh is also required. This approach is widely adopted in adaptive remeshing (see Chapters 4 and 5).

Since it is very common to use topology-preserving mesh moving algorithms in fluid–structure interaction applications, we provide a brief overview on some of the mesh moving algorithms. In a simple problem of fluid–structure interaction such as membrane–fluid interaction, often a one-dimensional membrane movement is assumed (no stretching). In such problems, assuming linear distribution of membrane movement in the direction of displacement is sufficient. For more complex problems and unstructured meshes, a horde of different methods are available. They include simple methods such as a spring analogy and Delaunay-based mapping to using solid mechanics equations to find out the mesh displacement. Some of them are briefly presented below.

13.3.3.1 *Spring analogy*

In this method the edges connecting two nodes are assumed to be connected by a spring that maintains equilibrium [40,41]. To find the position of a node a, the total force between node a and nodes connected to a is equal to zero to maintain equilibrium, i.e.,

$$\sum_{b=1}^{n_E} \mathbf{F}_{ab} = 0 \tag{13.70}$$

where n_E is the number of edges connected to node a. This may be written for a patch of elements as

$$\sum_{b=1}^{n_E} \mathbf{t}_{ab}^T k_{ab} \mathbf{t}_{ab}(\mathbf{u}_{ab}) = 0 \tag{13.71}$$

where k_{ab} is the spring constant connecting nodes a and b, which is often taken equal to the inverse of the square of the edge length $(= 1/l_{ab}^2)$, $\mathbf{t}_{ab}$ is the edge vector of edge ab given in two dimensions as

$$\mathbf{t}_{ab} = \begin{bmatrix} t_{a1} & t_{a2} & t_{b1} & t_{b2} \end{bmatrix}^T = \begin{bmatrix} \dfrac{\partial l_{ab}}{\partial x_{a1}} & \dfrac{\partial l_{ab}}{\partial x_{a2}} & \dfrac{\partial l_{ab}}{\partial x_{b1}} & \dfrac{\partial l_{ab}}{\partial x_{b2}} \end{bmatrix}^T$$

$$= \begin{bmatrix} -\cos\alpha & -\sin\alpha & \cos\alpha & \sin\alpha \end{bmatrix}^T \tag{13.72}$$

where subscripts 1 and 2 indicate the two Cartesian coordinate directions, and $\mathbf{u}_{ab}$ are the displacements and may be written for an edge as

$$\mathbf{u}_{ab} = \begin{bmatrix} u_{a1} & u_{a2} & u_{b1} & u_{b2} \end{bmatrix}^T \tag{13.73}$$

Although Eq. (13.71) is valid for a patch, the common practice is to solve the system for the whole mesh so that the boundary conditions can be easily applied on global boundaries. It is common to use a Gauss-Seidel method to solve a global equilibrium equation that puts all the patches together in the form

$$\mathbf{Ku} = \mathbf{0} \tag{13.74}$$

with known values of displacements along the boundaries. Here $\mathbf{K} = \mathbf{t}^T \mathbf{k} \mathbf{t}$. The above method of spring analogy is a good method for small displacements and fairly uniform meshes. However, the linear spring analogy discussed above has no control over the angle between edges. For keeping the angles between edges under control, the method needs to be modified by incorporating the torsional effects as well to the total force. The torsional force may be written for a node a as (assuming a triangle abc)

$$\mathbf{F}^t_{abc} = \mathbf{K}_{abc} \mathbf{u}_{abc} = 0 \tag{13.75}$$

The element stiffness matrix $\mathbf{K}_{abc}$ is now modified to incorporate the effects of torsion in terms of the angle between edges. This may be written as [following Eq. (13.71)]

$$\mathbf{K}_{abc} = \mathbf{R}^T_{abc} C_{abc} \mathbf{R}_{abc} \tag{13.76}$$

where $\mathbf{R}_{abc}$ is the rotation matrix and C_{abc} is the spring stiffness. The rotation matrix may be written as

$$\mathbf{R}_{abc} = \left[\begin{array}{ccc} \dfrac{\partial \theta_a}{\partial \mathbf{x}_a} & \dfrac{\partial \theta_a}{\partial \mathbf{x}_b} & \dfrac{\partial \theta_a}{\partial \mathbf{x}_c} \end{array} \right]^T \tag{13.77}$$

and the spring stiffness is given as

$$C_{abc} = \left(\frac{1}{1 - \cos \theta_a} \right) \left(\frac{1}{1 + \cos \theta_a} \right) = \left(\frac{1}{\sin^2 \theta_a} \right) \tag{13.78}$$

where θ_a is the angle between edges ab and ac. The stiffness is expressed in terms of $\sin \theta^2$ to restrict θ from reaching a value close to either 0° or 180°. What remains to be done is to compute the rotation matrix $\mathbf{R}_{abc}$. To compute this matrix for a triangle abc, we can write

$$\sin \theta_a = \frac{2A}{l_{ab} l_{ac}} \tag{13.79}$$

where A is the area of the triangle. Differentiating equation (13.79) with respect to any coordinate direction gives the following relation:

$$\frac{\partial \sin \theta_a}{\partial \mathbf{x}} = \cos \theta_a \frac{\partial \theta_a}{\partial \mathbf{x}} = \sin \theta \left[\frac{1}{A} \frac{\partial A}{\partial \mathbf{x}} - \frac{1}{l_{ab}} \frac{\partial l_{ab}}{\partial \mathbf{x}} - \frac{1}{l_{ac}} \frac{\partial l_{ac}}{\partial \mathbf{x}} \right] \tag{13.80}$$

Computing $\frac{\partial \theta_a}{\partial \mathbf{x}}$ using the above equation, the rotation matrix can be easily computed. The solution to the equilibrium equation can now be carried out using any standard procedure. It is also possible to sum the lineal force and torsional force together when applying the spring analogy to a problem in two or three dimensions.

13.3.3.2 *Mapping using background mesh (Delaunay graph method)*

This method follows a one-to-one mapping between the nodes and a background element [42]. The method starts with generation of a background mesh followed by allocation of the nodes of a finite element mesh to the background elements. A finite element node should only belong to one background element. As the structure moves within a fluid, the background mesh is moved with the structural movement. This is followed by the mapping of the nodes to the new position of the background element using simple finite element interpolation using barycentric (area) coordinates. Thus, the new position of a point within a background mesh may be written in terms of area coordinates as

$$\mathbf{x}_a = \sum_{b=1}^{3} L_b \mathbf{x}_b \qquad (13.81)$$

where L_b is the barycentric (area) coordinate of the background mesh calculated based on the original position of the node and the new position of the background element. For linear triangular elements this can simply be replaced with the shape functions. Although simple and robust for a problem with fairly uniform movement, certain difficulties are faced by the method if element nodes are shared between two background elements. For instance if two adjacent background elements are moving at much different rates, the element shared by these two background elements may be stretched or compressed excessively to create entanglement. Since the background mesh is often generated using the initial Delaunay triangulation, this method is sometimes referred as the Delaunay graph method.

### 13.3.3.3 *Solution to partial differential equations*

Though expensive, moving a mesh by solving an equilibrium equation appears to be robust [39]. The most general form of equation used in moving a mesh is an equation of elasticity. This is logical with displacement boundary conditions prescribed on the boundaries of a domain. The discrete form of the elasticity equation may be written as

$$\int_{\Omega_t} \mathbf{B}^T \mathbf{D} \mathbf{B} (\tilde{\mathbf{u}}^{n+1} - \tilde{\mathbf{u}}^n) \, d\Omega = \mathbf{F} \qquad (13.82)$$

where $\mathbf{B}$ is the matrix that contains the derivatives of shape functions (Chapter 3), $\mathbf{D}$ is the elasticity matrix, $\tilde{\mathbf{u}}$ is the vector of displacements within the fluid domain, and $\mathbf{F}$ contains the prescribed displacements on the solid surface. The matrix $\mathbf{D}$ may be simplified to $\frac{1}{A_e} \mathbf{I_m}$ with A_e being the area of elements and $\mathbf{I_m}$ is given for 3D as

$\mathbf{I_m} = \begin{bmatrix} 1 & & & & & \\ & 1 & & & & \\ & & 1 & & & \\ & & & 0 & & \\ & & & & 0 & \\ & & & & & 0 \end{bmatrix}$. This simplification reduces Eq. (13.82) to the vector form of a

Laplace-type equation. This may be employed to move a fluid mesh as shown in Fig. 13.8. This figure shows the movement of a rigid cylinder within a fluid domain. The
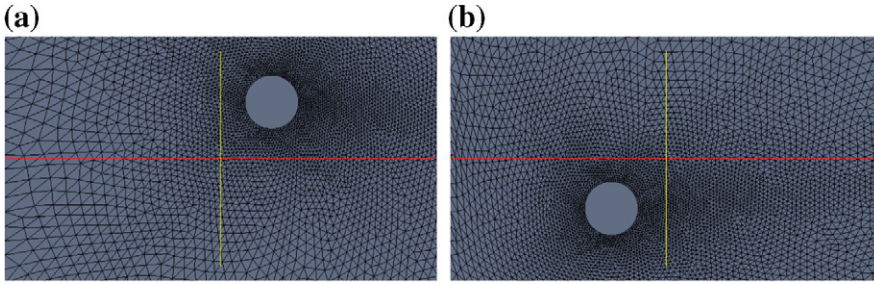
FIGURE 13.8

Artificially moved mesh surrounding a circular cylinder by solving the Laplace equation. (a) Cylinder moved to a position above and (b) below the original position.

cylinder here is artificially displaced to check the validity of the mesh moving method. As seen extreme movement of the mesh is possible for simple problems of this type. However, when the problem is complex and displacement is large, remeshing may be required to avoid mesh entanglement. Due to prohibitive cost involved with the remeshing, preserving topology is preferred in fluid–structure interaction problems.

13.3.3.4 *Other methods of mesh moving*

One of the very simple methods used for small displacements is the method of Laplacian smoothing. In this method the coordinate of a node is taken equal to the average of the coordinates surrounding that node, i.e.,

$$\mathbf{x}_a = \frac{1}{n_c} \sum_{b=1}^{n_c} \mathbf{x}_b \tag{13.83}$$

where n_c is the number of nodes connected to node a. This method works well if the displacement is much smaller than the element size. Often this method combined with a more general method provides better quality elements (see Fig. 13.9). On its own this method is unsuitable for boundary layer meshes and very fine meshes close to solid surfaces.

Another method for improving mesh quality used by researchers is minimization of the ratio between circumscribed and inscribed radii of a triangle (spheres in three dimensions), i.e., minimizing [33]

$$R_m = \sum_{ie=1}^{n_e} \left(\frac{r_{out}}{r_{in}} \right) \tag{13.84}$$

where n_e is the total number of elements in a mesh. Minimization may be carried out by differentiating R_m with respect to the nodal coordinates of the mesh, i.e.,

$$\frac{\partial R_m}{\partial \mathbf{x_a}} = 0 \tag{13.85}$$

with subscript a indicating all the nodes within the mesh.
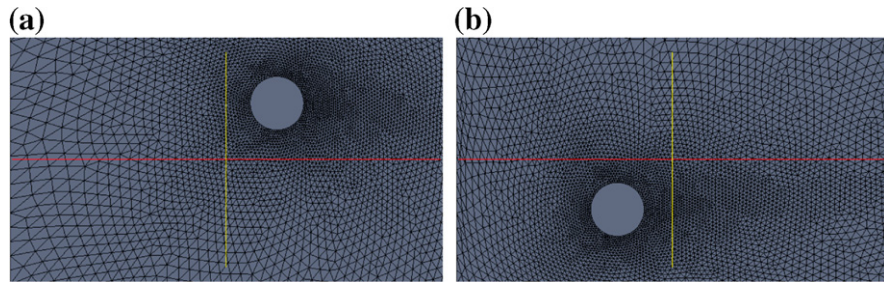
FIGURE 13.9

Artificially moved mesh surrounding a circular cylinder by solving the Laplace equation and applying Laplace smoothing. (a) Cylinder moved to a position above and (b) below the original position.

13.4 Concluding remarks

This chapter was intended as an introduction to the coupled problem of fluid–structure interaction. Although it is ideal to have a monolithic scheme for solving fluid–structure interaction, for various practical reasons a staggered approach is often preferred. However, for problems with added mass, it appears that monolithic schemes are as competitive as strongly coupled staggered approaches. Due to the evolving nature of this area, currently it is difficult to provide a firm conclusion. We hope that further progress will be made in this area in the next few years to get answers to some of the emerging questions on speed, accuracy, and robustness of solution methods for fluid–structure interaction problems.

References

[1] J.K. Raines, M.Y. Jaffrin, A.H. Shapiro, A computer simulation of arterial dynamics in the human leg, J. Biomech. 7 (1) (1974) 77–91.

[2] K.S. Rammos, G.J. Koullias, T.J. Papou, A.J. Bakas, P.G. Panagopoulos, S.G. Tsangaris, A computer model for the prediction of left epicardial coronary blood flow in normal, stenotic and bypassed coronary arteries, by single or sequential grafting, Cardiovascular Surgery 6 (6) (1998) 635–648.

[3] L. Formaggia, J.F. Gerbeau, F. Nobile, A. Quarteroni, On the coupling of 3D and 1D Navier-Stokes equations for flow problems in compliant vessels, Comput. Methods Appl. Mech. Eng. 191 (2001).

[4] L. Formaggia, F. Nobile, A. Quarteroni, A one dimensional model for blood flow: application to vascular prosthesis, in: I. Babuska, T. Miyoshi, P.G. Ciarlet (Eds.), Mathematical Modeling and Numerical Simulation in Continuum Mechanics,

Lecture Notes in Computational Science and Engineering, Springer-Verlag, Berlin, 2002.

[5] L. Formaggia, D. Lamponi, A. Quarteroni, One-dimensional models for blood flow in arteries, J. Eng. Math. 47 (2003) 251–276.

[6] S.A. Urquiza, P.J. Blanco, M.J. Vénere, R.A. Feijóo, Multidimensional modelling for the carotid artery blood flow, Comput. Methods Appl. Mech. Eng. 195 (33–36) (2006) 4002–4017.

[7] C. Sheng, S. Sarwal, K. Watts, A. Marble, Computational simulation of blood flow in human systemic circulation incorporating an external force field, Med. Biol. Eng. Comput. 33 (1) (1995) 8–17.

[8] S.J. Sherwin, L. Formaggia, J. Peiró, V. Franke, Computational modelling of 1D blood flow with variable mechanical properties and its application to the simulation of wave propagation in the human arterial system, Int. J. Numer. Methods Fluids 43 (6–7) (2003) 673–700.

[9] S.J. Sherwin, V. Franke, J. Peiró, K. Parker, One-dimensional modelling of a vascular network in space-time variables, J. Eng. Math. 47 (3) (2003) 217–250.

[10] J. Wan, B. Steele, S.A. Spicer, S. Strohband, G.R. Feijóo, T.J.R. Hughes, C.A. Taylor, A one-dimensional finite element method for simulation-based medical planning for cardiovascular disease, Comput. Methods Biomech. Biomed. Eng. 5 (3) (2002) 195–206.

[11] M.S. Olufsen, Structured tree outflow condition for blood flow in larger systemic arteries, Am. J. Physiol. 276 (1) (1999) H257–H268.

[12] M.S. Olufsen, C.S. Peskin, W.Y. Kim, E.M. Pedersen, A. Nadim, J. Larsen, Numerical simulation and experimental validation of blood flow in arteries with structured-tree outflow conditions, Ann. Biomed. Eng. 28 (2000) 1281–1299.

[13] S. Čanić, E.H. Kim, Mathematical analysis of the quasilinear effects in a hyperbolic model blood flow through compliant axi-symmetric vessels, Math. Methods Appl. Sci. 26 (14) (2003) 1161–1186.

[14] N.P. Smith, A.J. Pullan, P.J. Hunter, An anatomically based model of transient coronary blood flow in the heart, SIAM J. Appl. Math. 62 (3) (2002) 990–1018.

[15] S.J. Payne, Analysis of the effects of gravity and wall thickness in a model of blood flow through axisymmetric vessels, Med. Biol. Eng. Comput. 42 (2004) 799–806.

[16] G. Porenta, D.F. Young, T.R. Rogge, A finite-element model of blood flow in arteries including taper, branches, and obstructions, J. Biomech. Eng. 108 (2) (1986) 161–167.

[17] N. Stergiopulos, D.F. Young, T.R. Rogge, Computer simulation of arterial flow with applications to arterial and aortic stenoses, J. Biomech. 25 (12) (1992) 1477–1488.

[18] A.H. Shapiro, Steady flow in collapsible tubes, J. Biomech. Eng. 99 (1977) 126–147.

[19] C. Guiot, G. Pianta, C. Cancelli, T.J. Pedley, Prediction of coronary blood flow with a numerical model based on collapsible tube dynamics, Am. J. Physiol. 258 (1990) H1606–H1614.

[20] B.S. Brook, S.A.E.G. Falle, T.J. Pedley, Numerical solutions for unsteady gravity-driven flows in collapsible tubes: evolution and roll-wave instability of a steady state, J. Fluid Mech. 396 (1999) 223–256.

[21] P.J. Reuderink, H.W. Hoogstraten, P. Sipkema, B. Hillen, N. Westerhof, Linear and nonlinear one-dimensional models of pulse wave transmission at high Womersley numbers, J. Biomech. 22 (8–9) (1989) 819–827.

[22] T. Kitawaki, M. Shimizu, Flow analysis of viscoelastic tube using one-dimensional numerical simulation model, J. Biomech. Sci. Eng. 1 (1) (2006) 183–194.

[23] L. Formaggia, F. Nobile, A. Quarteroni, A. Veneziani, Multiscale modelling of the circulatory system: a preliminary analysis, Comput. Visual. Sci. 2 (2) (1999) 75–83.

[24] C. Hirsch, Numerical Computation of Internal and External Flows. II: Computational Method for Inviscid and Viscous Flows, Wiley Series in Numerical Methods in Engineering, John Wiley and Sons, Chichester, UK, 1990.

[25] M. Anliker, R.L. Rockwell, E. Ogden, Nonlinear analysis of flow pulses and shock waves in arteries. Part I: Derivation and properties of mathematical model, Z. Angew. Math. Phys. 22 (2) (1971) 217–246.

[26] O.C. Zienkiewicz, R.L. Taylor, J.Z. Zhu, The Finite Element Method: Its Basis and Fundamentals, seventh ed., Elsevier, Oxford, 2013.

[27] P. Causin, J.F. Gerbeau, F. Nobile, Added-mass effect in the design of partitioned algorithms for fluid–structure problems, Comput. Methods Appl. Mech. Eng. 194 (2005) 4506–4527.

[28] M. Heil, A.L. Hazel, J. Boyle, Solvers for large-displacement fluid–structure interaction problems: segregated versus monolithic approaches, Comput. Mech. 43 (2008) 91–101.

[29] J. Degroote, K.-J. Bathe, J. Vierendeels, Performance of a new partitioned procedure versus a monolithic procedure in fluid–structure interaction, Comput. Struct. 87 (2009) 793–801.

[30] U. Küttler, M. Gee, Ch. Förster, A. Comerford, W.A. Wall, Coupling strategies for biomedical fluid–structure interaction problems, Int. J. Numer. Methods Biomed. Eng. 26 (2010) 305–321.

[31] N. Newmark, A method of computation for structural dynamics, J. Eng. Mech., ASCE 85 (1959) 67–94.

[32] O.C. Zienkiewicz, R.L. Taylor, The Finite Element Method for Solid and Structural Mechanics, sixth ed., Elsevier, Oxford, 2005.

[33] W. Dettmer, D. Perić, A computational framework for fluid–structure interaction: finite element formulation and applications, Comput. Methods Appl. Mech. Eng. 195 (2006) 5754–5779.

[34] T.E. Tezduyar, S. Sathe, Modelling of fluid–structure interactions with the space-time finite elements: solution techniques, Int. J. Numer. Methods Fluids 54 (2007) 855–900.

[35] W.A. Wall, S. Genkinger, E. Ramm, A strong coupling partitioned approach for fluid–structure interaction with free surfaces, Comput. Fluids 36 (2007) 169–183.

[36] U. Küttler, W.A. Wall, Fixed-point fluid–structure interaction solvers with dynamic relaxation, Comput. Mech. 43 (2008) 61–72.

[37] T. Klöppel, A. Popp, U. Küttler, W.A. Wall, Fluid–structure interaction for non-conforming interfaces based on a dual mortar formulation, Comput. Methods Appl. Mech. Eng. 200 (2011) 3111–3126.

[38] D.C. Sternel, M. Schäfer, M. Heck, S. Yigit, Efficiency and accuracy of fluid–structure interaction simulations using an implicit partitioned approach, Comput. Mech. 43 (2008) 103–113.

[39] Y. Bazilevs, K. Takizawa, T.E. Tezduyar, Computational Fluid–Structure Interaction Methods and Applications, Wiley, 2013.

[40] C. Farhat, C. Degand, B. Koobus, M. Lesoinne, Torsional springs for two-dimensional dynamics unstructured fluid meshes, Comput. Methods Appl. Mech. Eng. 163 (1998) 231–245.

[41] C.O.E. Burg, A robust unstructured grid movement strategy using three-dimensional torsional springs, in: AIAA Paper 2004-2529, 2004.

[42] X. Liu, N. Qin, H. Xia, Fast dynamic grid deformation based on Delaunay graph mapping, J. Comput. Phys. 211 (2006) 405–423.